Edge-Hydroxylated Boron Nitride Nanosheets as an Effective Additive to Improve the Thermal Response of Hydrogels

*Feng Xiao, Sina Naficy, Gilberto Casillas, Majharul H. Khan, Tomas Katkus, Lei Jiang, Huakun Liu, Huijun Li, and Zhenguo Huang**

Isostructural to graphene, single-layer hexagonal boron nitride (*h*-BN) has alternating boron and nitrogen atoms replacing carbon atoms in an sp^2-bonded 2D layer.[1] Due to its atomically flat and electrically insulating surface, the *h*-BN nanosheets (BNNS) has been considered as an ideal substrate for graphene-based electronics.[2] In contrast to the covalent C–C bond of graphene, the ionic nature of the B–N bond makes BNNS highly resistant to oxidation (stable up to 840 °C in air)[3] and to corrosion.[4] Additionally, BNNS shows excellent mechanical properties and thus has been extensively applied as a lubricant in harsh environments.[5] More interestingly, BNNS has excellent thermal conductivity, which makes it an efficient filler to improve the thermal performance of liquids[6,7] and solid polymeric composites.[8] For all these applications, a facile method to synthesize high-quality BNNS is a prerequisite to take full advantage of its intrinsic properties.

The methods for the preparation of BNNS have been quite limited and inefficient, compared with the facile methods for the large-scale production of graphene. So far, the most common way of producing BNNS is via sonication-assisted exfoliation of bulk *h*-BN powder. To overcome the van der Waals forces between the layers, the liquid media/solvents for effective exfoliation should have similar surface energy to that of *h*-BN.[9] Mono- and few-layered BNNS have been prepared by sonicating *h*-BN in media such as water, isopropyl alcohol, and *N*-methyl-2-pyrrolidone.[10–12] A complete removal of some of the solvents, however, can be hampered by their high boiling points. Compared with the numerous reports on functionalized graphene, only a few papers have been published on functionalizing *h*-BN, which is likely due to its exceptional chemical stability. Simulations have indicated that effective functionalization of BNNS can change its band gap and consequently lead to applications in various fields.[13] Experimentally, hydroxyl functionalized BNNS (OH-BNNS) has been synthesized via various methods, including sonicating bulk *h*-BN powder in water,[10] heating bulk *h*-BN powder in air,[14] treating *h*-BN powder in hot $H_2SO_4/KMnO_4$ aqueous solution,[15] chemical reactions between *g*-C_3N_4 and $B(OH)_3$,[16] and oxygen radical functionalization followed by hydrolytic defunctionalization.[12] The presence of OH groups could alter the surface energy and thus ameliorate the solubility of BNNS in a variety of solvents. Being very common in nature, hydroxyl (OH) groups can interact with various forms of inorganic and organic matter, and therefore, the intrinsic properties of BNNS can be better exploited by grafting OH groups. For example, OH-BNNS has been very effective for polymer reinforcement[12] and drug delivery.[16]

Herein, we demonstrate a one-step route whereby commercial *h*-BN can be directly exfoliated by a steam treatment and simultaneously functionalized to yield OH-BNNS (**Figure 1**a). This procedure is simple, low cost, free of harsh chemicals, and can be readily scaled up. Furthermore, we demonstrate that the functionalization occurs predominantly along the platelet edge. The resultant excellent dispersion and stability of OH-BNNS in aqueous solution and organic solutions make it an effective additive to *N*-isopropylacrylamide-based hydrogels, leading to much enhanced thermal conductivity without compromising the mechanical properties. The resulting hydrogels demonstrate faster dimensional change and dye desorption upon heating.

Stable dispersions of ≈0.3 mg mL^{-1} OH-BNNS in water and ≈0.06 mg mL^{-1} OH-BNNS in ethanol (photographic images in Figure S1a,b, preparation process in the Supporting Information) appear translucent, and the concentrations are much higher than those for BNNS with negligible amounts of hydroxyl groups[17] and are consistent with previous reports.[7,10,14] The scanning electron microscopy (SEM) studies show that the as-received *h*-BN (Figure S2, Supporting Information) powders consist of thick platelets with smooth

F. Xiao, M. H. Khan, T. Katkus, Prof. H. Liu, Dr. Z. Huang
Institute for Superconducting and Electronic Materials
University of Wollongong
Wollongong, NSW 2500, Australia
E-mail: zhenguo@uow.edu.au
Dr. S. Naficy
Intelligent Polymer Research Institute and ARC Centre of Excellence for Electromaterials Science
University of Wollongong
Wollongong, NSW 2500, Australia
Dr. G. Casillas
Electron Microscopy Center
University of Wollongong
Wollongong, NSW 2500, Australia
Prof. L. Jiang
Beijing National Laboratory of Molecular Sciences (BNLMS)
Key Laboratory of Organic Solids
Institute of Chemistry
Chinese Academy of Sciences
Beijing 100190, P.R. China
Prof. H. Li
School of Mechanical, Materials and Mechatronic Engineering
University of Wollongong
Wollongong, NSW 2500, Australia

DOI: 10.1002/adma.201502803

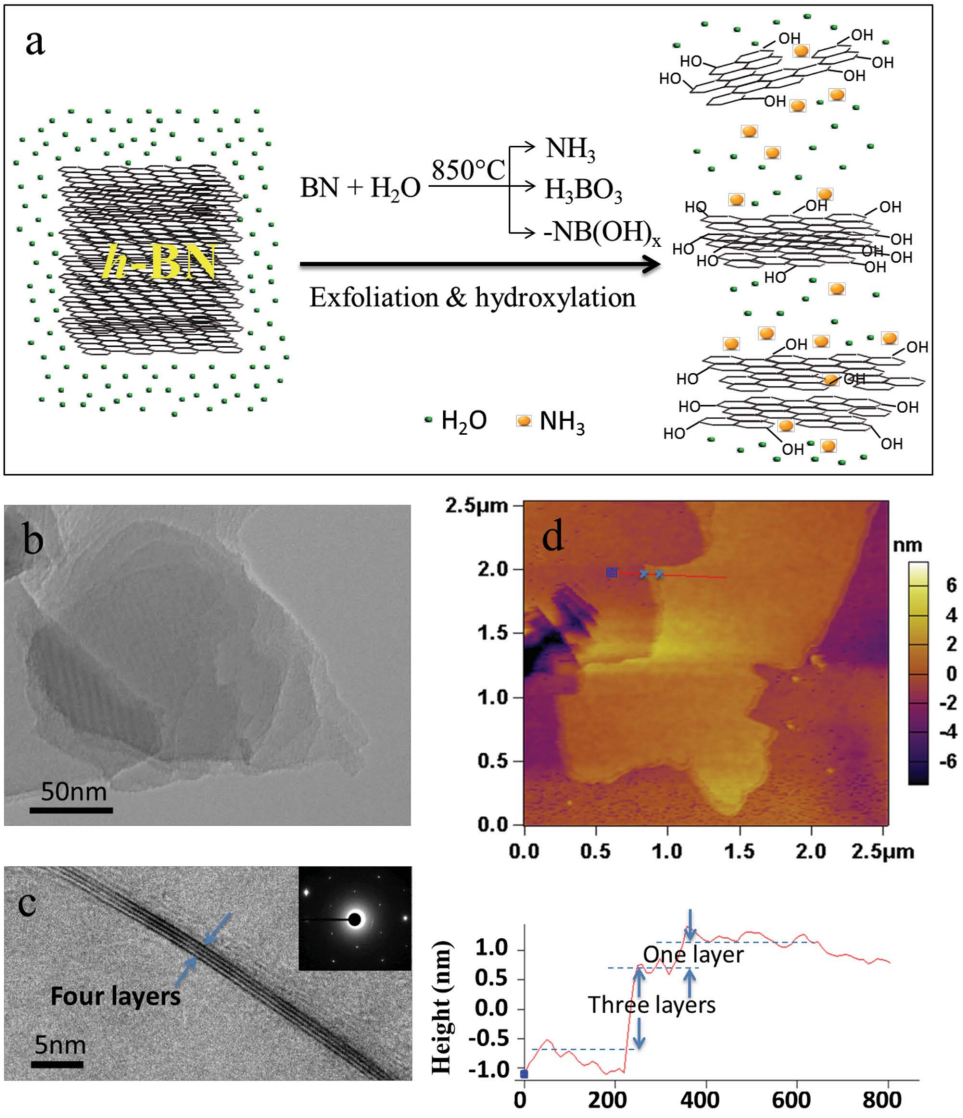

Figure 1. a) Schematic illustration of hydrolysis-assisted exfoliation and hydroxylation of *h*-BN powder in hot steam, where H_2O reacts with *h*-BN, forming NH_3 and $–NB(OH)_x$, and the highly energetic H_2O and NH_3 assist the exfoliation through diffusion between BN layers; b) TEM image of a Moiré pattern due to the stacking of few-layered OH-BNNS; c) TEM image of four-layered OH-BNNS (inset showing the corresponding electron diffraction pattern); d) AFM topographic image and the corresponding height profile of OH-BNNS showing a terraced morphology with a monolayered OH-BNNS joined to a trilayered OH-BNNS.

surfaces and edges, and the lateral size is from 1 to 7 μm. The OH-BNNS (Figure S2a–c, Supporting Information) obtained at 850 °C appears to be transparent due to the much reduced thickness, but with a slightly reduced lateral size ranging from sub-micrometer to several micrometers. This is much larger than the exfoliated OH-BNNS in previous reports.[10,14,17] When the temperature was increased to 1000 °C, smaller sheets with more noticeable voids in the plane were obtained (Figure S2d,e, Supporting Information). This morphology is very similar to that in previous reports,[14,17] where prolonged sonication was applied to exfoliate the *h*-BN. The formation of small sheets with many defects will have a negative impact on the heat transfer along the plane. Therefore, a low temperature, 850 °C in this case, has been selected to produce large OH-BNNS with fewer defects.

Figure 1b shows transmission electron microscopy (TEM) images of OH-BNNS with morphology similar to the parent *h*-BN powder. The Moiré pattern is associated with the restacked few-layered OH-BNNS with different orientations, which has been observed in the case of graphene.[18] Few-layered OH-BNNS can be clearly seen in high-magnification TEM images (Figure 1c and Figure S2f, Supporting Information). The electron diffraction pattern (inset of Figure 1c) reveals the typical sixfold symmetry of *h*-BN, indicative of the structural integrity after the exfoliation. Atomic force microscopy (AFM) topographic images of OH-BNNS were acquired via tapping mode. Isolated OH-BNNS with a thickness of ≈1 nm and a lateral size of ≈2 μm was observed (Figure 1d). A terraced morphology showing a monolayered OH-BNNS joined to a trilayered OH-BNNS can be seen, taking into account the solvents trapped

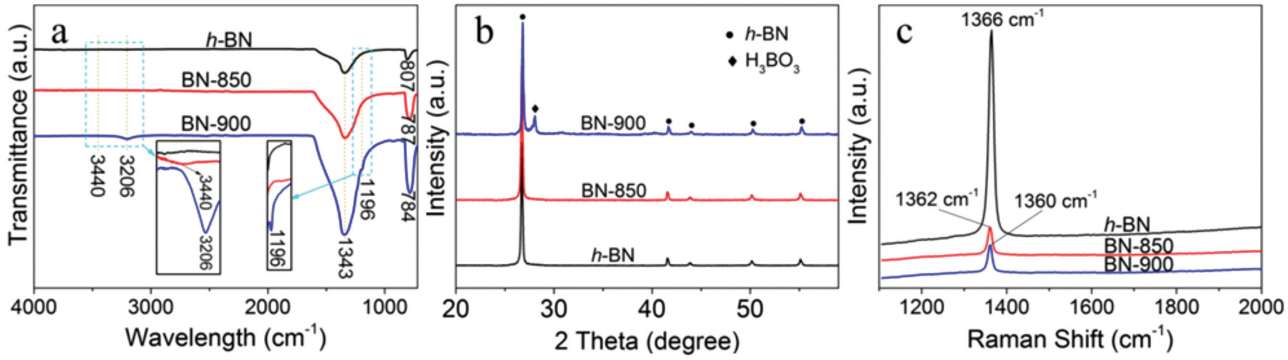

Figure 2. Pristine *h*-BN and *h*-BN treated at 850 °C (denoted as BN-850) and 900 °C (BN-900). a) FTIR spectra showing the presence of only –NB(OH)$_x$ in BN-850, as opposed to the large amount of H_3BO_3 in BN-900; b) XRD patterns revealing the presence of H_3BO_3 in BN-900, which is negligible in BN-850. c) The redshifts in the Raman spectra of the E_{2g} peak indicate the formation of few-layered BN at elevated temperatures.

between the OH-BNNS and the silicon substrate.[19] The result is in good agreement with that in Figure 1c, further supporting the effective exfoliation of *h*-BN during the treatment.

Similar to other nitrides, including Si_3N_4, TiN, and CrN, *h*-BN is also sensitive to moisture at elevated temperatures, due to the strong affinity of N toward O in H_2O.[20] After the heat treatment under hot steam, white ammonium pentaborate tetrahydrate ($NH_4B_5O_8\cdot 4H_2O$) powder is deposited on the inner wall of the quartz tube downstream of the Ar outlet,[21] as confirmed by the X-ray diffraction (XRD) analysis (Figure S3, Supporting Information). The initially pure deionized water in the disposal unit has a high level of ammonia, as confirmed by the Nessler's reagent test (Figure S4, Supporting Information). The overall reaction can be described in Equation (1), which has also been observed before.[10,22] The formation of $NH_4B_5O_8\cdot 4H_2O$ is due to the reaction between NH_3 and H_3BO_3.

$$BN + H_2O \rightarrow NH_3 + B(OH)_3 \quad (1)$$

The exfoliation is facilitated by the hydrolysis reaction at these high temperatures with the release of ammonia gas. The high thermal input at these temperatures would weaken the van der Waals forces between the BN layers. The hot H_2O gradually reacts with *h*-BN, forming voids (size depending on the temperature and reaction duration) on the (002) basal plane and along the edges, which would further weaken the van der Waals forces. The highly dynamic H_2O and NH_3 formed in situ at such high temperatures may therefore penetrate through these voids and diffuse slowly between the BN layers, causing exfoliation, as evidenced by the SEM and TEM images (Figure 1b,c). AFM was used to measure the statistical thickness of the OH-BNNS[11] (Figure S1c, Supporting Information), which confirms that the final product has a thickness that mainly varies from 1 to 5 nm, with ≈20% being 1–2 nm and over 60% being 3–4 nm. This method gives a high yield of >30% for few-layered BNNS in the products. The yield of OH-BNNS could be controlled by optimizing the synthesis temperature and reaction duration. We found that the reaction rate is slow at 850 °C and the weight loss is only 5% in 2 h, suggesting that at this stage, the majority of BN nanosheets remain as the solid product. Higher temperatures contribute to the formation of boric acid and consequently reduce the yields (Table S1 and S2, Supporting Information).

The functionalization occurs simultaneously with the hydrolysis, as illustrated in Figure 1a. The driving force of the reaction is believed to be the formation of NH_3 as a leaving group. The exposed B atoms with dangling bonds then react with hydroxyl groups. The reaction in Equation (1) describes a situation where charge neutral H_3BO_3 is formed. In reality, tetrahedrally coordinated $N_3B(OH)$ is also formed.[16] The presence of —B(OH) can be verified using Fourier transform infrared (FTIR) spectroscopy.[10,12,23]

Two strong FTIR bands at ≈1343 cm^{-1} and ≈807 cm^{-1} are present in pristine *h*-BN, *h*-BN treated at 850 °C (BN-850), and *h*-BN treated at 900 °C (BN-900) (**Figure 2**a), which are correlated with the in-plane stretching and the out-of-plane bending mode of *h*-BN, respectively.[24] The redshifts from 807 cm^{-1} for pristine *h*-BN to 787 cm^{-1} for BN-850, and 784 cm^{-1} for BN-900, are due to the disruption by hydroxyl groups, which leads to vibration at lower wavenumber.[12] A peak at 3440 cm^{-1}, assigned to the O–H stretching mode from the $N_3B(OH)$ unit, appears in the BN-850, which is consistent with previous results.[10,12,15,16] Reactions at lower temperatures would not lead to an observable band at 3440 cm^{-1} (not shown here). For the BN-900, the O–H stretching mode at 3206 cm^{-1} and a new bending mode at 1200 cm^{-1} appear simultaneously, which are correlated with H_3BO_3, where boron is triangularly coordinated with oxygen.[25] This is confirmed by the XRD pattern (Figure 2b) of BN-900, where diffraction peaks associated with H_3BO_3 are clearly visible.[14] Based on the results obtained, we propose the following explanation. H_3BO_3 has a low decomposition point (≈170 °C), but under the hot steam in the quartz tube, it can survive high temperatures. Additionally, it also has a low boiling point of 300 °C, so it could evaporate away quickly. Based on the $NH_4B_5O_8\cdot 4H_2O$ white powder obtained at the downstream outlet of the tube (for all the temperatures), it can be reasoned that most of the H_3BO_3 has been evaporated away. At 850 °C, the evaporation rate is relatively faster than the formation rate of H_3BO_3, leaving no H_3BO_3 in the final product. At 900 °C, a reverse trend occurs, and H_3BO_3 was observed in the final product, as confirmed by FTIR and XRD. The reactions were tried at higher temperatures with more H_3BO_3 observed in the final product (Table S1,

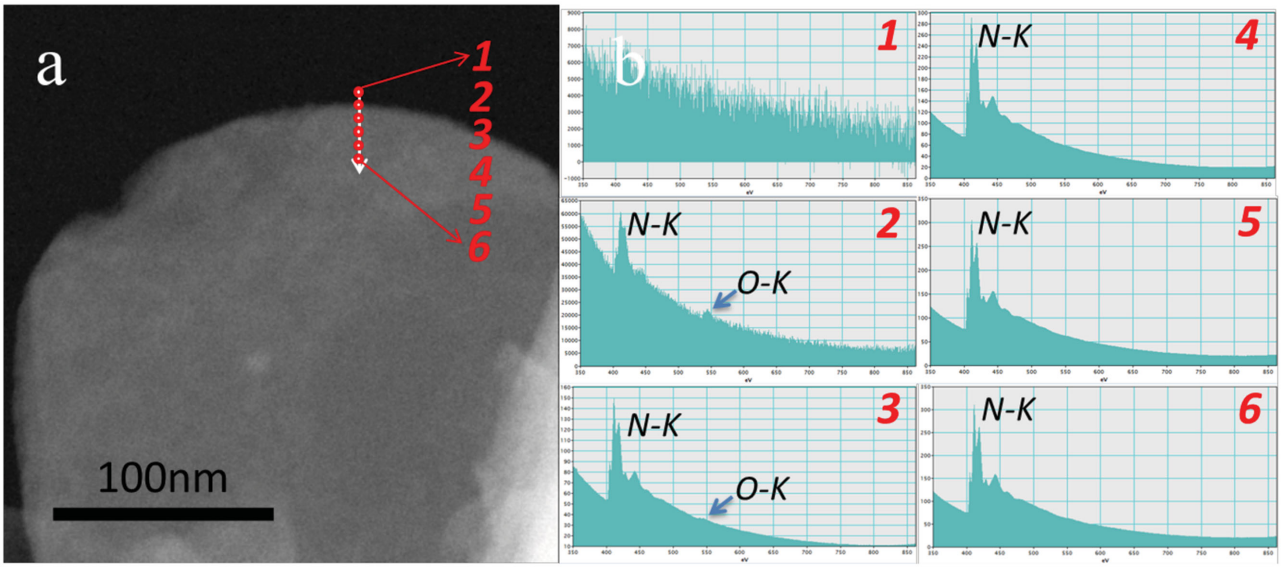

Figure 3. EELS mapping shows that the hydroxyl groups are predominately located along the edges of the nanosheets. Area 1 is off the BNNS so no O–K or N–K peak is observed; on moving to the edge of the BNNS (area 2), the O–K peak appears and then becomes weaker on moving away from the edge (area 3). The O–K peak is not observed when moving further into the basal plane (areas 4–6). The presence of 1s–π^* and 1s–σ^* peaks of the N–K edge confirm that the intrinsic hexagonal structure of *h*-BN still remains.

Supporting Information). Therefore, by adopting the optimum temperature, 850 °C in this case, OH-BNNS can be obtained with an undetectable amount of impurities after a single heat treatment. Furthermore, the resultant OH-BNNS can be directly dispersed in solvents to be used as additives, avoiding tedious purification processes such as washing, centrifuging, and drying, which have been typically applied in the preparation of OH-BNNS.[12,17,26] The Raman spectra (Figure 2c) contain bands at 1362 cm^{-1} (BN-850) and 1360 cm^{-1} (BN-900), close to 1366 cm^{-1} for the commercial *h*-BN, all of which can be attributed to the E_{2g} mode vibration of *h*-BN. The slight red-shifts of 4 cm^{-1} (BN-850) and 6 cm^{-1} (BN-900) in relation to that of the pristine *h*-BN are another piece of evidence that the bulk *h*-BN has been exfoliated to produce predominantly few-layered nanosheets, which feature reduced interlayer interactions and shortening of the B–N bond.[12]

FTIR and X-ray photoelectron spectroscopy have been often used to validate the formation of OH-BNNS, but the location of OH groups on the plane has been vaguely described.[12,15,23] Aberration-corrected STEM is one of the most powerful tools to characterize matter at the sub-nanometer level. It is typically coupled with energy-dispersive X-ray spectroscopy (EDS) to unequivocally identify elements present in the structure. EDS, however, is not reliable for light elements (O and lighter) due to many experimental factors. This limitation is overcome by the use of electron energy loss spectroscopy (EELS), where the light elements can be detected with the same resolution as the microscope. Here, we have employed EELS to probe the location of the OH groups in the BN sheets (**Figure 3**). Note that in this high-angle annular dark field STEM image, the edge has the same intensity as the interior of the sheet, indicating that it is not a folding but a flat edge. We can see the O–K peak at ≈532 eV in areas 2 and 3, which are along the edges of the OH-BNNS, and the disappearance of the O–K peak in areas 4–6, which are away from the edges, suggesting that the BNNS have been functionalized predominately on the edges rather than on the basal plane (Figure S5, Supporting Information). In addition, the presence of 1s–π^* and 1s–σ^* peaks of the N–K edge confirms that the intrinsic hexagonal structure of *h*-BN still remains.

Herein, we demonstrate the use of OH-BNNS as an effective additive to enhance the thermal response of poly(*N*-isopropylacrylamide) (PNIPAM) hydrogel. PNIPAM is one of the most widely studied temperature-sensitive hydrogels, with applications ranging from drug delivery to various types of smart systems.[27] The efficacy of these applications is highly dependent on the critical response of the hydrogel to changes in temperature, which in most cases needs to be extremely fast. To take full advantage of the high thermal conductivity of *h*-BN as an additive, it is critical to well disperse the *h*-BN in the hydrogel network, which is not easy due to its hydrophobicity. In this work, the Raman mapping indicates that OH-BNNS is uniformly embedded in the hydrogel matrix rather than forming scattered aggregates (**Figure 4**c,d). The excellent dispersion can be ascribed to the extensive hydrogen bond network between the hydroxyl groups on the BNNS and *N*-isopropylacrylamide (Figure 4a). Such a uniform distribution would effectively favor the exploitation of the high intrinsic thermal conductivity of the BNNS, which consequently enhances heat transfer throughout the hydrogel network.

As a well-known temperature-sensitive hydrogel, PNIPAM becomes opaque and shrinks at the same time when heated above ≈32 °C. It returns to its initial state when the temperature is reduced below the transition temperature. A faster change in opacity and size indicates a better temperature response, which is critical for practical applications. Such an improvement was observed in the response of our PNIPAM/OH-BNNS hydrogels to temperature changes. The addition of only 0.07 wt% (based

ADVANCED MATERIALS
www.advmat.de

www.MaterialsViews.com

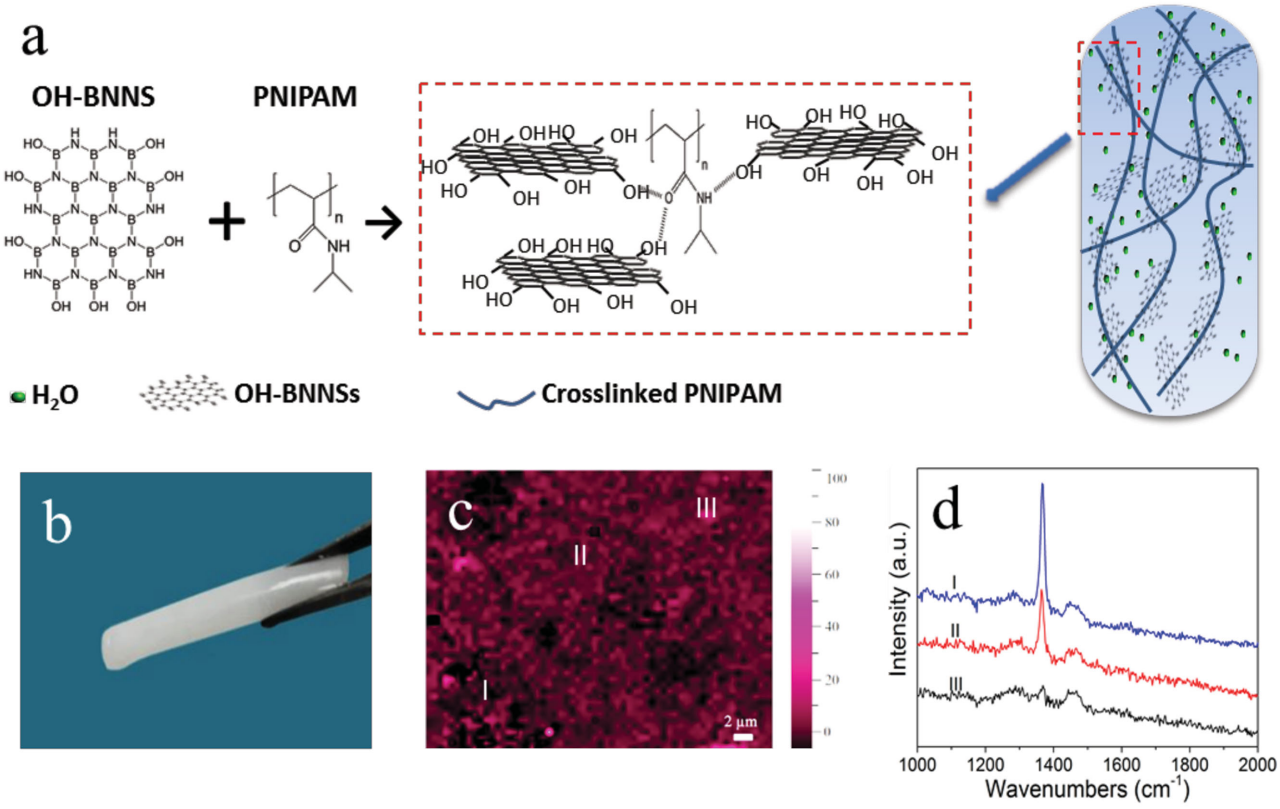

Figure 4. a) Schematic illustration of the formation of PNIPAM/OH-BNNS hydrogel, where the crosslinked PNIPAM and OH-BNNS are integrated through hydrogen bonding; b) photographic image of PNIPAM/OH-BNNS hydrogel; c) Raman mapping collected at 1362 cm^{-1}, showing the uniform distribution of the OH-BNNS in the hydrogel network; and d) Raman spectra of three points with maximum (III), mean (II), and minimum (I) intensity, judged by human eyes. The featured peaks of PNIPAM (at ≈1450 cm^{-1}) and OH-BNNS (≈1360 cm^{-1}) have an independent existence.

on polymer precursor) OH-BNNS to the hydrogel improved the thermal conductivity by 41% (**Figure 5**a). When the PNIPAM/OH-BNNS hydrogel composite and pure PNIPAM were taken out of warm water at 50 °C, the former showed a much faster change in transparency than the latter, with a maximum 40% margin (Figure 5b), indicative of the pivotal role of OH-BNNS in the thermal enhancement.

As the dimensions of the hydrogel have an inverse temperature dependence, another test was carried out to compare the rate of the length change of cylindrical samples when the temperature was increased from room temperature to 50 °C. Both hydrogels were made under the exact same conditions with the same dimensions. The PNIPAM/OH-BNNS hydrogel composite shows faster length change (inset in Figure 5c). Specifically, the greatest difference in length appears at 30 s, when the hydrogel composite has shrunk to 3.8 from 4.2 cm, a fivefold greater shrinking rate than that of its neat counterpart, which has shrunk from 4.2 to 4.15 cm. Finally, after 6 min, the lengths of both hydrogels are nearly the same. The faster response rate is attributed to the highly improved thermal conductivity across the composite due to the presence of OH-BNNS sheets. This faster change in dimension would make the PNIPAM/OH-BNNS hydrogel composite a better candidate for actuator applications (e.g., valves) that work by thermal stimulation.

Dye release from the hydrogels was also tested, which provides a simple simulation of the releasing process for drug solutions. Since PNIPAM hydrogels undergo large volume deformation upon heating, the drug molecules can be "squeezed" out of the hydrogel composite. Blue dye (blue food coloring) was loaded on both neat and composite hydrogels in the same Petri dish until both reached equilibrium with an identical dark blue color, as perceived by human eyes. They were then put into warm water (T = 40 °C) for dye release. After 0.5 min, the PNIPAM/OH-BNNS hydrogel began releasing the dye, while the neat hydrogel showed no detectable change in color (Figure 5d). At 3 min, the color of the PNIPAM/OH-BNNS hydrogel became a lighter blue, indicating that more dye had been released during the same period than for the neat hydrogel. The faster dye release upon temperature change again indicates that the well-dispersed OH-BNNS improves heat conductivity. PNIPAM/OH-BNNS hydrogels therefore could show a prompt response to their environmental temperature to deliver drug solutions more effectively than the corresponding neat ones.

As discussed above, the treatment of bulk *h*-BN powder at high temperatures under steam leads to simultaneous exfoliation and functionalization of the *h*-BN. The resultant OH-BNNS is edge-modified and hydrophilic enough to form good suspensions in water and alcohol. Moreover, when mixed with polymers soluble in water or alcohol, the OH groups on the nanosheet edges appear to be conducive to a collective interaction between the BNNS and the polymer, most likely through hydrogen bonding, and thus, no phase segregation takes

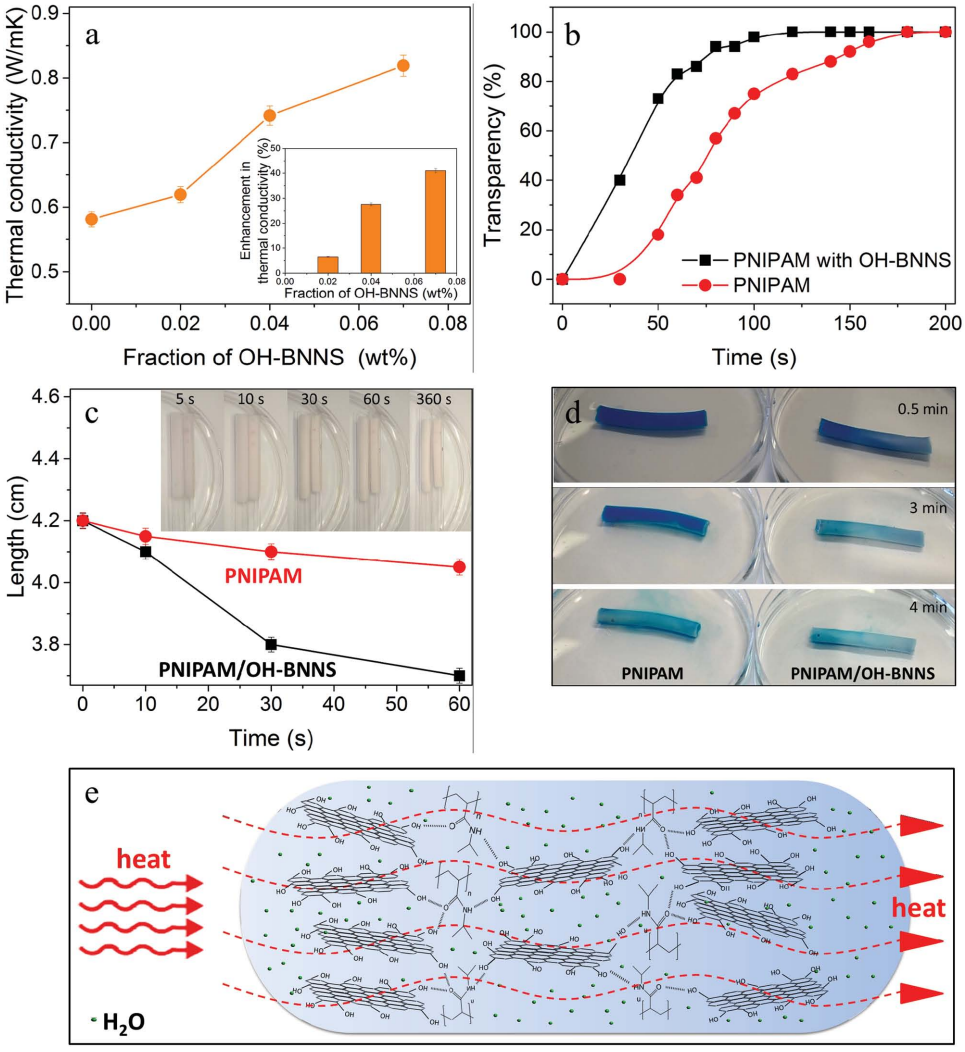

Figure 5. a) Thermal conductivity improvement with the increasing ratio of OH-BNNS (inset: the improvement by percentage), b) change in transparency, c) change in length of cylindrical samples (inset: photographs of hydrogels at different times, with PNIPAM on the left and PNIPAM/OH-BNNS on the right), d) dye release upon heating, and e) schematic illustration of the enhanced heat transfer in PNIPAM/OH-BNNS hydrogel, which has resulted from the excellent integration between the OH-BNNS, H_2O, and the crosslinked PNIPAM through hydrogen bonding.

place. This is evidenced by the Raman mapping collected at 1362 cm^{-1} (Figure 4c,d), which reveals a uniform distribution of BNNS across the hydrogel network. It is important to note that there is no obstacle to using other hydrophilic monomers and polymers to prepare hydrogel composites, so long as the precursors are soluble in water or ethanol. Indeed, we were able to successfully make uniform poly(ethylene glycol)/OH-BNNS and poly(hydroxyethylmethacrylate)/OH-BNNS composites.

It is well known that water–PNIPAM interaction and water–water interaction in the hydrogel is highly sensitive to changes in temperature. Below the lower critical solution temperature (LCST), hydrophilic amide (–NH), and carbonyl (–CO) groups form hydrogen bonds with water molecules, with the interaction dominated by an enthalpic term. Once above the LCST, the entropic gain overcomes the enthalpic term, and water molecules are released.[27] How to effectively transfer the heat to "all" the molecules so to speed up their response is critical for any thermal-stimulus applications. These intermolecular hydrogen bond interactions between water and OH-BNNS, as well as PNIPAM and OH-BNNS, allow the OH-BNNS to act as a thermal carrier to continuously and effectively diffuse the heat throughout the hydrogel composite matrix (Figure 5e), which consequently enhances the thermally stimulated performance of PNIPAM/OH-BNNS hydrogel according to the tests above. The absence of –OH groups on the basal plane is also advantageous, since otherwise, deformation of the BNNS plane would occur, especially in the case of hydrogen bonding. We have also found that OH-BNNS can effectively improve the thermal conductivity of the NIPAM/water mixture and even pure water (Table S3, Supporting Information), which is critical since the hydrogel contains a large amount of water (>80% by weight). The improvement is likely due to the high phonon transport along the OH-BNNS basal planes.[6,28] The interfacial thermal contact resistance is minimized due to the large contact area between the OH-BNNS and the polymer, as well as the water. In addition, the close interaction through hydrogen

bonding will effectively facilitate the transport of phonons between the BN sheets. We believe that the presence of OH groups has not appreciably perturbed the crosslinking efficiency of the hydrogel, which significantly affects the response time when the temperature is changed. The swelling (change in mass) ratio of the hydrogel remained unchanged, ≈9.2 ± 0.1, when OH-BNNS was added (at the concentration range studied here). No change was observed in the LCST of the polymer (all around 32 °C) upon adding OH-BNNS. In addition, the shrinkage ratios of the hydrogels with and without OH-BNNS are the same, although the rates of dimensional change are different (Figure 5d). Therefore, the thermal enhancement is predominantly caused by the incorporated OH-BNNS.

A simple simulation (Figure S7, Supporting Information) indicates that the experimental data are close to those predicted using a parallel conduction model.[29] It should be noted that, in the parallel model, the conductive filler is arranged in parallel with the direction of thermal flux, which is the most ideal case. It should be noted that the thermal contacts between any interfaces are normally poor. We have confirmed the good dispersion of OH-BNNS in the hydrogel composite with excellent contact between the OH-BNNS and PNIPAM hydrogel through hydrogen bonding. The thermal conductivity of OH-BNNS used for modeling is 360 W m^{-1} K^{-1}, which is the experimental value for 11-layered *h*-BN with trace of poly(methyl methacrylate) (PMMA), and it was suggested that the ineffective removal of the PMMA residue would degrade the thermal performance.[30] It should also be noted that thermal conductivity of single-layered *h*-BN can be over 1000 W m^{-1} K^{-1}.[31] In our case, there is a proportion of few-layered, including monolayer, OH-BNNS, which could contribute more thermal enhancement than relatively thick OH-BNNS. It is thus likely that the experimental value of the 0.04 wt% loading is close to the simulated value.

The hydrogels need to maintain suitable mechanical properties for practical applications. All polymerization solutions made with OH-BNNS dispersions remained stable for several days until they were polymerized, after which, the nanosheets were fully locked into the network. Over five tests, no significant improvement in the Young's modulus was observed when OH-BNNS was incorporated into the hydrogel formulation. Some improvements were obtained from compression testing of the hydrogel composites, where PNIPAM/OH-BNNS hydrogels exhibited a higher compression strength and final strain (Figure S8, Supporting Information).

Notably, BNNS is known to be non-cytotoxic and has been studied for therapeutic or diagnostic applications.[16,32] The PNIPAM/OH-BNNS hydrogel composite is not expected to be cytotoxic either. Therefore, the dramatic improvement in the response to external heat stimulation could be very beneficial for a wide range of bionic and soft robotic applications.

In summary, we have developed a facile and scalable method to directly exfoliate and functionalize intrinsically hydrophobic bulk *h*-BN into hydrophilic OH-BNNS. The hydroxyl groups are predominantly located along the edges of the nanosheets rather than on the basal plane. The excellent dispersibility of OH-BNNS in water and alcohol makes it an effective additive to hydrogels. The intrinsic thermal properties have been perfectly inherited, since the resultant OH-BNNS exhibited large and few-layered morphology rather than the small fragments produced by the sonication-based exfoliation. The PNIPAM/OH-BNNS hydrogel composite shows a much faster thermal response compared to the bare hydrogel, with a 41% improvement in thermal conductivity achieved by adding only 0.07 wt% OH-BNNS. The hydrogel composite also shows faster dimensional change upon heating, with the discrepancy proving that OH-BNNS has passed on its excellent thermal properties to the PNIPAM hydrogel. Most interestingly, the dye-release test demonstrates its improved drug-delivery capability. According to the merits above, our PNIPAM/OH-BNNS with its superior thermal response is envisaged to be a promising candidate in the field of bionic and soft robotic applications.

Supporting Information

Supporting Information is available from the Wiley Online Library or from the author.

Acknowledgements

F.X. gratefully acknowledges the Chinese Scholarship Council (CSC) for his scholarship. Z.H. is the recipient of an Australian Research Council Discovery Early Career Research Award (project number DE120101496). S.N. acknowledges the Global Challenges program of the University of Wollongong for funding. This research used equipment located in the UOW Electron Microscopy Centre that was funded by an Australian Research Council (ARC) Linkage, Infrastructure, Equipment, and Facilities (LIEF) grant (LE120100104).

Received: June 10, 2015
Revised: August 5, 2015
Published online: October 26, 2015

[1] a) A. Pakdel, Y. Bando, D. Golberg, *Chem. Soc. Rev.* **2014**, *43*, 934; b) X.-F. Jiang, Q. Weng, X.-B. Wang, X. Li, J. Zhang, D. Golberg, Y. Bando, *J. Mater. Sci. Technol.* **2015**, *31*, 589.
[2] a) M. Wang, S. K. Jang, W.-J. Jang, M. Kim, S.-Y. Park, S.-W. Kim, S.-J. Kahng, J.-Y. Choi, R. S. Ruoff, Y. J. Song, S. Lee, *Adv. Mater.* **2013**, *25*, 2746; b) W. Yang, G. Chen, Z. Shi, C.-C. Liu, L. Zhang, G. Xie, M. Cheng, D. Wang, R. Yang, D. Shi, K. Watanabe, T. Taniguchi, Y. Yao, Y. Zhang, G. Zhang, *Nat. Mater.* **2013**, *12*, 792.
[3] L. H. Li, J. Cervenka, K. Watanabe, T. Taniguchi, Y. Chen, *ACS Nano* **2014**, *8*, 1457.
[4] M. Yi, Z. Shen, X. Zhao, S. Liang, L. Liu, *Appl. Phys. Lett.* **2014**, *104*, 143101.
[5] D.-H. Cho, J.-S. Kim, S.-H. Kwon, C. Lee, Y.-Z. Lee, *Wear* **2013**, *302*, 981.
[6] J. Taha-Tijerina, T. N. Narayanan, G. Gao, M. Rohde, D. A. Tsentalovich, M. Pasquali, P. M. Ajayan, *ACS Nano* **2012**, *6*, 1214.
[7] W.-L. Song, P. Wang, L. Cao, A. Anderson, M. J. Meziani, A. J. Farr, Y.-P. Sun, *Angew. Chem.* **2012**, *124*, 6604.
[8] a) C. Zhi, Y. Bando, C. Tang, H. Kuwahara, D. Golberg, *Adv. Mater.* **2009**, *21*, 2889; b) X.-B. Wang, Q. Weng, X. Wang, X. Li, J. Zhang, F. Liu, X.-F. Jiang, H. Guo, N. Xu, D. Golberg, Y. Bando, *ACS Nano* **2014**, *8*, 9081; c) X. Wang, C. Zhi, L. Li, H. Zeng, C. Li, M. Mitome, D. Golberg, Y. Bando, *Adv. Mater.* **2011**, *23*, 4072; d) H. Zhu, Y. Li, Z. Fang, J. Xu, F. Cao, J. Wan, C. Preston, B. Yang, L. Hu, *ACS Nano* **2014**, *8*, 3606; e) C. Zhi, Y. Xu, Y. Bando, D. Golberg, *ACS Nano*

2011, *5*, 6571; f) X. Wang, A. Pakdel, J. Zhang, Q. Weng, T. Zhai, C. Zhi, D. Golberg, Y. Bando, *Nanoscale Res. Lett.* **2012**, *7*, 662.

[9] J. N. Coleman, M. Lotya, A. O'Neill, S. D. Bergin, P. J. King, U. Khan, K. Young, A. Gaucher, S. De, R. J. Smith, I. V. Shvets, S. K. Arora, G. Stanton, H.-Y. Kim, K. Lee, G. T. Kim, G. S. Duesberg, T. Hallam, J. J. Boland, J. J. Wang, J. F. Donegan, J. C. Grunlan, G. Moriarty, A. Shmeliov, R. J. Nicholls, J. M. Perkins, E. M. Grieveson, K. Theuwissen, D. W. McComb, P. D. Nellist, V. Nicolosi, *Science* **2011**, *331*, 568.

[10] Y. Lin, T. V. Williams, T.-B. Xu, W. Cao, H. E. Elsayed-Ali, J. W. Connell, *J. Phys. Chem. C* **2011**, *115*, 2679.

[11] K. R. Paton, E. Varrla, C. Backes, R. J. Smith, U. Khan, A. O'Neill, C. Boland, M. Lotya, O. M. Istrate, P. King, T. Higgins, S. Barwich, P. May, P. Puczkarski, I. Ahmed, M. Moebius, H. Pettersson, E. Long, J. Coelho, S. E. O'Brien, E. K. McGuire, B. M. Sanchez, G. S. Duesberg, N. McEvoy, T. J. Pennycook, C. Downing, A. Crossley, V. Nicolosi, J. N. Coleman, *Nat. Mater.* **2014**, *13*, 624.

[12] T. Sainsbury, A. Satti, P. May, Z. Wang, I. McGovern, Y. K. Gun'ko, J. Coleman, *J. Am. Chem. Soc.* **2012**, *134*, 18758.

[13] a) Q. Tang, Z. Zhou, P. Shen, Z. Chen, *Chem. Phys. Chem.* **2013**, *14*, 1787; b) Q. Tang, J. Bao, Y. Li, Z. Zhou, Z. Chen, *Nanoscale* **2014**, *6*, 8624.

[14] Z. Cui, A. J. Oyer, A. J. Glover, H. C. Schniepp, D. H. Adamson, *Small* **2014**, *10*, 2352.

[15] G. R. Bhimanapati, D. Kozuch, J. A. Robinson, *Nanoscale* **2014**, *6*, 11671.

[16] Q. Weng, B. Wang, X. Wang, N. Hanagata, X. Li, D. Liu, X. Wang, X. Jiang, Y. Bando, D. Golberg, *ACS Nano* **2014**, *8*, 6123.

[17] X. Li, X. Hao, M. Zhao, Y. Wu, J. Yang, Y. Tian, G. Qian, *Adv. Mater.* **2013**, *25*, 2200.

[18] Y. Hernandez, V. Nicolosi, M. Lotya, F. M. Blighe, Z. Sun, S. De, I. T. McGovern, B. Holland, M. Byrne, Y. K. Gun'Ko, J. J. Boland, P. Niraj, G. Duesberg, S. Krishnamurthy, R. Goodhue, J. Hutchison, V. Scardaci, A. C. Ferrari, J. N. Coleman, *Nat. Nano* **2008**, *3*, 563.

[19] a) Y. Lin, J. W. Connell, *Nanoscale* **2012**, *4*, 6908; b) S. Park, R. S. Ruoff, *Nat. Nanotechnol.* **2009**, *4*, 217.

[20] a) S. Motojima, Y. Tamura, K. Sugiyama, *Thin Solid Films* **1982**, *88*, 269; b) C. G. Cofer, J. Economy, *Carbon* **1995**, *33*, 389.

[21] T. Matsuda, *J. Mater. Sci.* **1989**, *24*, 2353.

[22] T. Saito, F. Honda, *Wear* **2000**, *237*, 253.

[23] a) A. S. Nazarov, V. N. Demin, E. D. Grayfer, A. I. Bulavchenko, A. T. Arymbaeva, H.-J. Shin, J.-Y. Choi, V. E. Fedorov, *Chem. Asian J.* **2012**, *7*, 554; b) Y. Lin, T. V. Williams, W. Cao, H. E. Elsayed-Ali, J. W. Connell, *J. Phys. Chem. C* **2010**, *114*, 17434.

[24] R. Geick, C. H. Perry, G. Rupprecht, *Phys. Rev.* **1966**, *146*, 543.

[25] S. Anderson, R. L. Bohon, D. D. Kimpton, *J. Am. Ceram. Soc.* **1955**, *38*, 370.

[26] M. Du, X. Li, A. Wang, Y. Wu, X. Hao, M. Zhao, *Angew. Chem. Int. Ed.* **2014**, *53*, 3645.

[27] a) Y. Qiu, K. Park, *Adv. Drug Delivery Rev.* **2012**, *64*, 49; b) X. Zhang, C. L. Pint, M. H. Lee, B. E. Schubert, A. Jamshidi, K. Takei, H. Ko, A. Gillies, R. Bardhan, J. J. Urban, M. Wu, R. Fearing, A. Javey, *Nano Lett.* **2011**, *11*, 3239; c) C. Yu, Z. Duan, P. Yuan, Y. Li, Y. Su, X. Zhang, Y. Pan, L. L. Dai, R. G. Nuzzo, Y. Huang, H. Jiang, J. A. Rogers, *Adv. Mater.* **2013**, *25*, 1541.

[28] C. Zhi, Y. Bando, T. Terao, C. Tang, H. Kuwahara, D. Golberg, *Adv. Funct. Mater.* **2009**, *19*, 1857.

[29] Y. Agari, T. Uno, *J. Appl. Polym. Sci.* **1986**, *32*, 5705.

[30] I. Jo, M. T. Pettes, J. Kim, K. Watanabe, T. Taniguchi, Z. Yao, L. Shi, *Nano Lett.* **2013**, *13*, 550.

[31] L. Lindsay, D. A. Broido, *Phys. Rev. B* **2011**, *84*, 155421.

[32] a) X. Chen, P. Wu, M. Rousseas, D. Okawa, Z. Gartner, A. Zettl, C. R. Bertozzi, *J. Am. Chem. Soc.* **2009**, *131*, 890; b) L. Horváth, A. Magrez, D. Golberg, C. Zhi, Y. Bando, R. Smajda, E. Horváth, L. Forró, B. Schwaller, *ACS Nano* **2011**, *5*, 3800.